nature materials

ARTICLES

https://doi.org/10.1038/s41563-021-01148-3

Fabrication and nanophotonic waveguide integration of silicon carbide colour centres with preserved spin-optical coherence

Charles Babin[1], Rainer Stöhr[1], Naoya Morioka[1,2], Tobias Linkewitz[1], Timo Steidl[1], Raphael Wörnle[1], Di Liu[1], Erik Hesselmeier[1], Vadim Vorobyov[1], Andrej Denisenko[1], Mario Hentschel[3], Christian Gobert[4], Patrick Berwian[4], Georgy V. Astakhov[5], Wolfgang Knolle[6], Sridhar Majety[7], Pranta Saha[7], Marina Radulaski[7], Nguyen Tien Son[8], Jawad Ul-Hassan[8], Florian Kaiser[1]✉ and Jörg Wrachtrup[1]

Optically addressable spin defects in silicon carbide (SiC) are an emerging platform for quantum information processing compatible with nanofabrication processes and device control used by the semiconductor industry. System scalability towards large-scale quantum networks demands integration into nanophotonic structures with efficient spin–photon interfaces. However, degradation of the spin-optical coherence after integration in nanophotonic structures has hindered the potential of most colour centre platforms. Here, we demonstrate the implantation of silicon vacancy centres (V_{Si}) in SiC without deterioration of their intrinsic spin-optical properties. In particular, we show nearly lifetime-limited photon emission and high spin-coherence times for single defects implanted in bulk as well as in nanophotonic waveguides created by reactive ion etching. Furthermore, we take advantage of the high spin-optical coherences of V_{Si} centres in waveguides to demonstrate controlled operations on nearby nuclear spin qubits, which is a crucial step towards fault-tolerant quantum information distribution based on cavity quantum electrodynamics.

Quantum information distribution enables provably secure communication[1], blind quantum computing[2] and advanced quantum metrology[3]. Large-scale quantum networks can be realized based on a well-orchestrated interplay between stationary and flying multi-qubit systems[4]. In this regard, by addressing atom-like transitions in optically active solid-state spins[5,6], impressive landmark demonstrations showed multi-node quantum networks[7], quantum error correction[8] and entanglement distillation[9].

To claim system scalability, the field has yet to improve the interaction between colour centres and photons. For example, the emission of an optical dipole usually covers a solid angle of 4π, and the associated low light collection efficiency results in slow experimental rates[10], reduced single-shot readout fidelity and limited quantum protocol complexity. Near-deterministic light–matter interaction is achieved via colour centre integration into monolithic resonators[11–13]. A challenge remains to preserve spin-optical coherence while granting high-fidelity access to qubit clusters, such as nuclear spins. The nitrogen vacancy centres in diamond[14] and divacancy spins in SiC[15] showed excellent control over nuclear spins. However, integration into nanophotonics structures proved challenging as spin-optical coherences are degraded by coupling to nearby spins and charge traps, which can be present in the starting material and/or be formed during nanofabrication[13,16–21]. Group-IV defects in diamond show robust symmetry-protected optical coherences[22,23], but high-fidelity spin manipulation requires millikelvin temperatures at which direct control over nuclear spin clusters becomes challenging[24,25].

By contrast, deep-bulk V_{Si} centres in 4H-SiC have shown excellent optical coherences up to $T = 20$ K due to wavefunction symmetry protection[26,27], with millisecond spin-coherence times[28] and coherent coupling to nuclear spins[29]. This has led to the demonstration of a coherent light–matter interface comprising one electron spin and two photons, suitable for cluster state generation[30]. The single dipole orientation of V_{Si} centres facilitates integration into nanophotonic resonators; however, little is known about spin-optical coherences in such structures.

Here, we demonstrate that V_{Si} centres retain excellent spin-optical properties after generation via helium (He) ion implantation, which allows for three-dimensional positioning. Compared to previous approaches based on either heavy ions (mass above He ions) or at high acceleration voltages (>10 keV)[31–34], we use low-energy ions to create shallow V_{Si} centres with a yield of 8%. We show nearly lifetime-limited absorption lines and record Hahn echo spin-coherence times. Further, we simulate SiC waveguide designs[35] and create triangular cross-section nanophotonic waveguides via reactive ion etching (RIE). For V_{Si} centres in such waveguides, we report nearly lifetime-limited absorption lines without degradation of spin coherences compared to defects in bulk

[1]3rd Institute of Physics, IQST, and Research Centre SCoPE, University of Stuttgart, Stuttgart, Germany. [2]Institute for Chemical Research, Kyoto University, Uji, Japan. [3]4th Institute of Physics, IQST, and Research Centre SCoPE, University of Stuttgart, Stuttgart, Germany. [4]Fraunhofer Institute for Integrated Systems and Device Technology IISB, Erlangen, Germany. [5]Helmholtz-Zentrum Dresden-Rossendorf, Institute of Ion Beam Physics and Materials Research, Dresden, Germany. [6]Department of Sensoric Surfaces and Functional Interfaces, Leibniz-Institute of Surface Engineering (IOM), Leipzig, Germany. [7]Department of Electrical and Computer Engineering, University of California, Davis, CA, USA. [8]Department of Physics, Chemistry and Biology, Linköping University, Linköping, Sweden. ✉e-mail: f.kaiser@pi3.uni-stuttgart.de

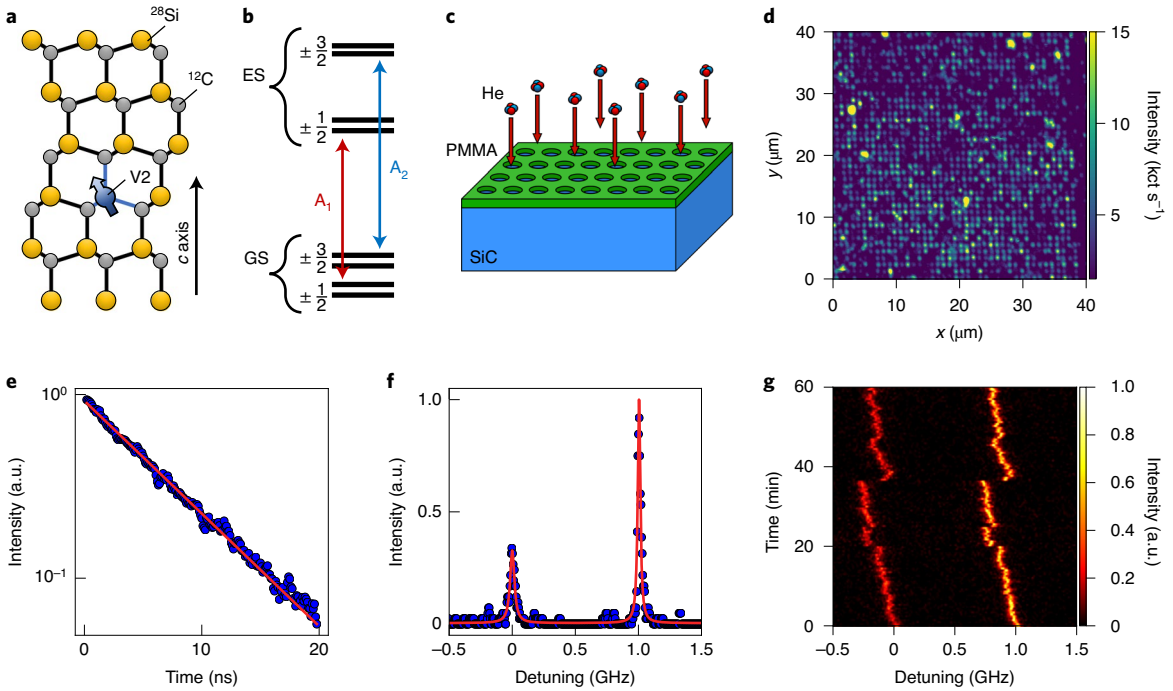

Fig. 1 | Properties of He$^+$ ion-implanted V2 centres. a, Crystal structure of 4H-SiC. The V2 centre is formed by a missing silicon atom at a cubic lattice site. **b**, Energy level diagram of V2 centres. Ground (GS) and excited states (GS) are spin quartets and optical transitions are spin conserving (A_1, red; A_2, blue). **c**, Schematics of V2 centre creation via He$^+$ ion implantation. He$^+$ ions are accelerated to 6 keV and implanted at the *a* side of the crystal through a lithographed PMMA mask. **d**, Confocal fluorescence scan of the implanted defect centre array. kct s^{-1}, kilocounts per second. **e**, Off-resonant excitation lifetime measurement of a single V2 centre. The fit is based on a single-exponential decay (proportional to $\exp(-t/\tau)$) with a 1/e lifetime of $\tau = 7.08 \pm 0.06$ ns. **f**, Single-scan resonant photoluminiscence excitation scan on an implanted V2 centre. The nearly lifetime-limited linewidth confirms the excellent spectral stability of V2 centres. **g**, Repeated resonant excitation scans during 1 h without repump laser. No ionization is observed and the small remaining drift is assigned to surface charge fluctuations. a.u., arbitrary units.

material. Capitalizing on those advances, we coherently control nearby nuclear spins with near-unity fidelity, which represents a significant step forward towards integrated multi-spin, multi-photon clusters.

V_{Si} generation through low-energy He$^+$ ion implantation

We investigate the cubic lattice site silicon vacancy centre (V2) in 4H-SiC (Fig. 1a). V2 centres are characterized by a zero-phonon line (ZPL) at 917 nm, with a Debye–Waller factor (DWF) of 8–9% (refs. [26,36]). As shown in Fig. 1b, the system is spin-$\frac{3}{2}$, in which the sublevels $m_S = \pm\frac{1}{2}$ and $m_S = \pm\frac{3}{2}$ are degenerate Kramers doublets[37]. Optical transitions are spin conserving, resulting in two absorption lines, labelled A_1 and A_2, respectively[38].

As shown in Fig. 1c, we generate arrays of V_{Si} centres via implantation of He$^+$ ions. They are sent through a polymethyl methacrylate (PMMA) mask with 100 nm diameter holes, lithographed on the *a* face of an epitaxially grown SiC sample with a low nitrogen concentration in the [N] = 4×10^{13} cm^{-3} range (for more details, see Sample preparation). Compared to previous work[31–34,39,40], we choose a low He$^+$ ion energy of 6 keV to minimize crystal damage. To remove residual lattice damage, we subsequently anneal the sample in argon atmosphere at 600 °C for 30 min. Figure 1d shows the room-temperature photoluminescence map of an implanted array using off-resonant excitation at 785 nm. We infer the defect number per spot using autocorrelation measurements and obtain a Poissonian distribution with a mean value of 0.67 ± 0.06 V2 centres per spot. Considering the ion dose of 1×10^{11} cm^{-2}, we determine an implantation yield of 8.5 ± 0.8%, similar to previous work[34]. From the fluorescence map, we infer that the implanted defect centres are laterally distributed with a variance of ±54 nm (1 s.d.), which is mainly determined by the implantation mask hole size. Synopsys Sentaurus Monte Carlo simulations show that V2 centres are created about 30–40 nm beneath the surface without channelling effects (Section 1A of the Supplementary Information and Supplementary Figs. 1 and 2).

Although high-accuracy shallow defect generation is crucial for integration into nanophotonic resonator devices and for quantum sensing applications, it has remained unclear whether spin-optical coherences can be maintained after ion implantation[32,34]. For many colour centres, ion implantation and surface proximity lead to strong degradation of spin-optical properties[41–43]. Here, we show that V2 centres do not suffer from these problems.

To benchmark the quality of the resonant absorption linewidths, we first measure the excited state lifetime of a single V2 centre at a temperature of $T = 10$ K with a 780 nm picosecond-pulsed pump laser. The data in Fig. 1e reveal a single-exponential decay with a 1/e lifetime of $\tau = 7.08 \pm 0.06$ ns, similar to previous work[39]. Thus, the lifetime-limited absorption linewidth is $\Delta\nu = (2\pi\tau)^{-1} = 22.5 \pm 0.2$ MHZ. Additional data for proton and silicon ion implantation are given in Section 1B of the Supplementary information and Supplementary Figs. 4–6.

Subsequently, we perform resonant excitation with a tunable diode laser at 917 nm (Toptica DL pro). We provide an additional microwave (MW) drive at 70 MHz to continuously mix the ground states[29], and in this way counteract optical spin-pumping[38]. A typical resonant photoluminescence excitation scan is shown in Fig. 1f. The two absorption lines show the previously shown separation of 1 GHz (ref. [26]). The fitted linewidths are $\Delta\nu_{A_1} = 41 \pm 2$ MHz and $\Delta\nu_{A_2} = 24 \pm 1$ MHz for the A_1 and A_2 transitions, respectively, which are close to the lifetime limit. A long-term absorption line

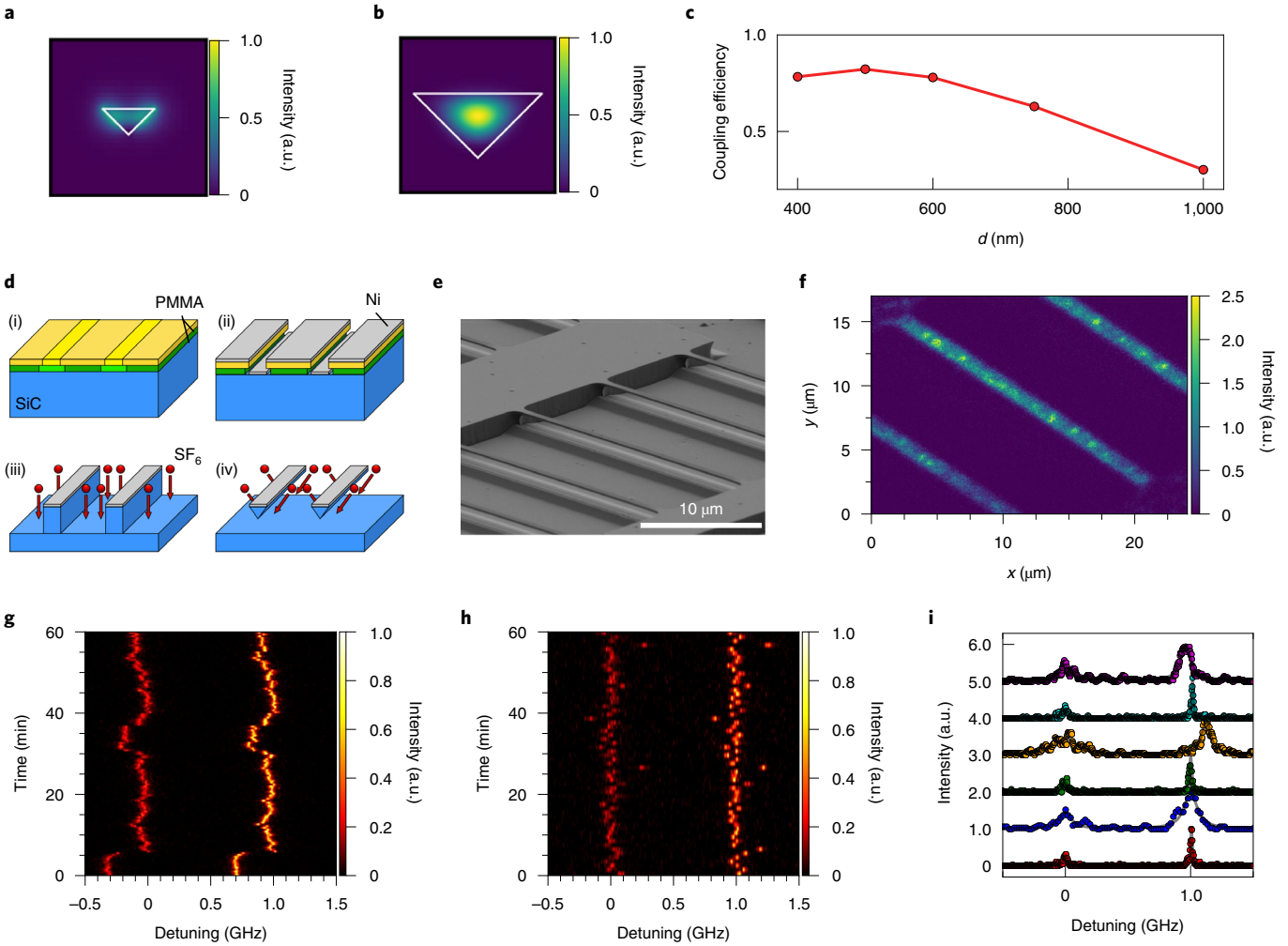

Fig. 2 | Properties of V2 centres in nanofabricated waveguides. a, Cross-sectional fundamental TE mode profile in waveguides with a half-opening angle α = 45° and width d = 400 nm. **b**, TE mode profile for a waveguide with α = 45° and d = 1,000 nm. **c** Coupling efficiency into the fundamental TE waveguide mode as a function of the width d (with emitter assumed to be located in the centre of the waveguide). High efficiencies are reached for d = 400–600 nm. **d**, Waveguide fabrication recipe. (i) Deposition of a double layer of PMMA mask; (ii) deposition of a nickel mask; (iii) a straight reactive ion etch based on SF_6 plasma creates 3 μm deep trenches; (iv) an angled SF_6 plasma etch creates triangular cross-section waveguides. **e**, Scanning electron microscope image of the created waveguide structures that appear smooth and well undercut. **f**, Confocal fluorescence microscope image of the waveguides. Bright spots are, in the majority, surface-related defects. On average, one V2 centre is found in every five waveguides with d = 1,000 nm. **g**, Resonant excitation scans over 1 h. No ionization is observed and the wavelength drift is minimal. **h**, Resonant excitation scans with the laser feedback software activated once per minute. **i**, Single-line resonant excitation scans for six different V2 centres in waveguides. For better visibility, the A_1 transition for all spectra is centred at zero detuning. The actual spectral distribution of the defects is ±10 GHz, which is comparable to bulk defects[56].

measurement is shown in Fig. 1g, revealing little drift with no signs of ionization. Averaging over 125 scans, we find a linewidth of 40 MHz (29 MHz) for the A_1 (A_2) transition, with a distribution (1 s.d.) of 10 MHz (5 MHz), respectively. Those measurements corroborate the excellent stability of the V2 centre optical lines. We highlight that these results are reproducible for other V2 defects (Section 1A of the Supplementary Information and Supplementary Fig. 3).

Spin-optical performance of V_{Si} centres in nanophotonic waveguides

We now proceed to V2 centres in nanofabricated waveguides[44,45]. We focus on triangular cross-section waveguides, with which high cooperativity cavities have been realized[46]. Additionally, this geometry is very versatile and can be directly applied to bulk substrates of any polytype, without the need for doping level engineering[13]. In colour centre integration with triangular waveguides, single-mode light propagation is crucial for quantum applications. The relationship between device profile and its supported mode wavelength has been modelled recently[35]. Here, we expand on those findings and simulate light propagation in triangular cross-section waveguides with a half-opening angle of α = 45° (Supplementary Information). Figure 2a,b shows the fundamental transverse electric (TE) modes that are supported by waveguides with widths of d = 400 nm and d = 1,000 nm, respectively. Figure 2c shows the coupling efficiency of light emitted by a centrally located horizontally polarized dipole at 917 nm into the fundamental transverse electric (TE) mode as a function of d. For d = 500 nm, we find high coupling efficiencies up to 82% (41% in each propagation direction). The d = 1,000 nm device still shows a good coupling efficiency of 30% while some of the out-scattered fluorescence can be detected from the top of the waveguide with our collection optics.

To ensure that the V2 centre dipole is parallel to the top surface of the waveguides and to highlight reproducibility across different SiC crystals, we now use a different epitaxially grown SiC layer.

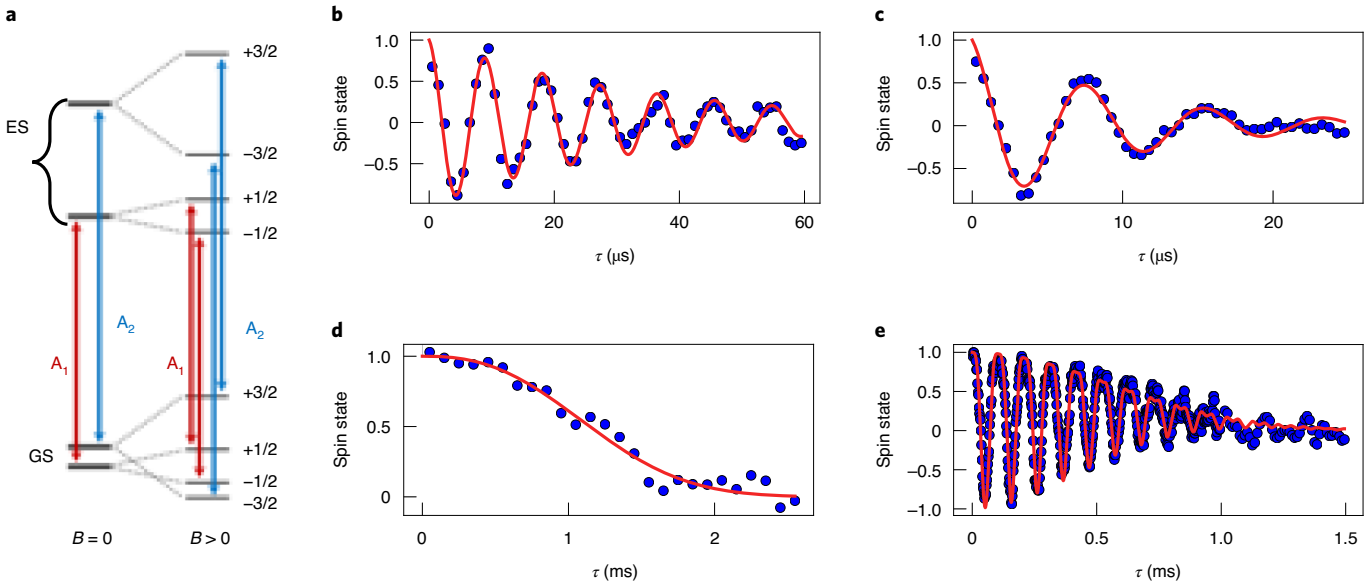

Fig. 3 | Electron spin properties of nanofabricated V2 centres. a, Energy level diagram of V2 centres in an external magnetic field to lift the Kramers degeneracy in the ground and excited states. **b**, Ramsey interferometry for He$^+$ implanted V2 centres. The dephasing time is $T^*_{2,\mathrm{implanted}} = 34 \pm 4$ μs. **c**, Dephasing of V2 centres in waveguides, $T^*_{2,\mathrm{waveguide}} = 9.4 \pm 0.7$ μs. **d**, Spin-coherence time of He$^+$ implanted V2 centres using Hahn echo. The coherence time is $T_{2,\mathrm{implanted}} = 1.39 \pm 0.06$ ms. **e**, Spin-coherence in waveguides, $T_{2,\mathrm{waveguide}} = 0.84 \pm 0.01$ ms. The strong modulation corroborates coupling to at least one nearby ^{29}Si nuclear spin. In all plots, spin state +1 corresponds to $m_S = \frac{3}{2}$ and −1 to $m_S = \frac{1}{2}$. The signal envelopes are fitted using stretched exponential functions proportional to $A \exp\left(-\frac{t}{\tau}\right)^N + y_0$.

The sample was grown along the *a* side with a slightly higher nitrogen concentration, $[\mathrm{N}] \approx 3 \times 10^{15}\,\mathrm{cm}^{-3}$. Before nanofabrication, we create V2 centres throughout the entire sample at a density of 0.4 $\mu\mathrm{m}^{-3}$ using electron irradiation at 2 MeV with a dose of 2 kGy (with fluence of approximately $5 \times 10^{11}\,\mathrm{cm}^{-2}$).

To fabricate waveguide devices, we decide against photoelectrochemical etching, which may deteriorate spin-optical properties due to material degradation and porosification[13]. As shown in Fig. 2d, we fabricate triangular cross-section waveguides via a two-stage process based on RIE with SF_6 gas. An initial straight etch creates ~2 μm deep trenches. Subsequent angled etching in a 45° Faraday cage results in suspended waveguide structures with a length of 20 μm and widths of 400 nm and 1,000 nm, respectively. A scanning electron microscope image of the latter ones is shown in Fig. 2e.

A typical photoluminescence map with optical excitation and collection from the top of the waveguides is shown in Fig. 2f, revealing multiple bright spots along the waveguides. Emission spectra reveal most of the spots as surface-related or unknown defects (Supplementary Information). Bright single V2 centres are found in one out of five waveguides with 1,000 nm width. Intuitively, this is low compared to the average V2 density in the bulk. However, our simulations show that only emitters at the waveguides' top apices show a sizable emission towards our collection optics. The fluorescence of most emitters is actually guided along the waveguides or out-scattered towards the bottom (Section 3 of the Supplementary Information and Supplementary Figs. 15 and 16). In analogy to the measurements on implanted V2 centres, we perform resonant photoluminescence excitation scans. Figure 2g shows a 1-h-long recording, revealing narrow absorption lines with no signs of ionization. Considering that we primarily investigate defects at the waveguide apices, we assign the remaining slow drift to surface charge fluctuations.

To demonstrate that the drift is slow enough to perform complex long-term measurements, we stabilize the resonant excitation laser on optical transitions via software-control[47] (Section 2E of the Supplementary Information and Supplementary Fig. 11). Figure 2h shows absorption line scans repeated over 1 h with the laser feedback activated once per minute and re-centring of the scanning window after every scan with respect to the position of the A_1 transition. Little to no effective drift is observed[19,41], which enables long-term measurements. To highlight reproducibility, we show the resonant absorption spectra of V2 centres in six different waveguides in Fig. 2i. We find that three out of six V2 centres show nearly lifetime-limited absorption lines. The other three still present spin-selective optical transitions. The best defect shows a linewidth of 34 MHz (22 MHz) for the A_1 (A_2) transition, after averaging over 198 scans. The standard deviation in these measurements is 8 MHz (5 MHz). Unfortunately, we did not identify V2 centres in the 400-nm-wide devices. We attribute this to the single-mode operation of the 400 nm waveguides, which suppresses out-scattering towards our collection optics, thus requiring dedicated output couplers[22,48].

The next step should combine nanofabrication and localized defect generation, for which multiple strategies exist, such as waveguide fabrication around precharacterized implanted defect arrays or depositing He$^+$ ion implantation masks on produced waveguides. For the 45° etched waveguides, both strategies require precise alignment in the range of a few 10 nm. Our simulations indicate reduced demands on alignment in single-mode devices with a wider opening angle (75° and 900–1,000 nm width; Section 2G of the Supplementary Information and Supplementary Figs. 13 and 14). Such devices could be created with adapted Faraday cages. Based on the success in the diamond platform[11,46], we believe that mask-free implantation would be ideal, which can be achieved using a helium focussed ion beam source or a helium ion microscope operated at fluxes of about ten He$^+$ ions per spot.

Nuclear spin control with waveguide-integrated V_{Si} centres

Having demonstrated implantation and nanofabrication with minimal degradation of the optical properties of V2 centres, we proceed to spin-coherence measurements. To maximize spin contrast, we use resonant excitation[29] and take advantage of our software-controlled laser feedback system. Intuitively, we expect that spin properties

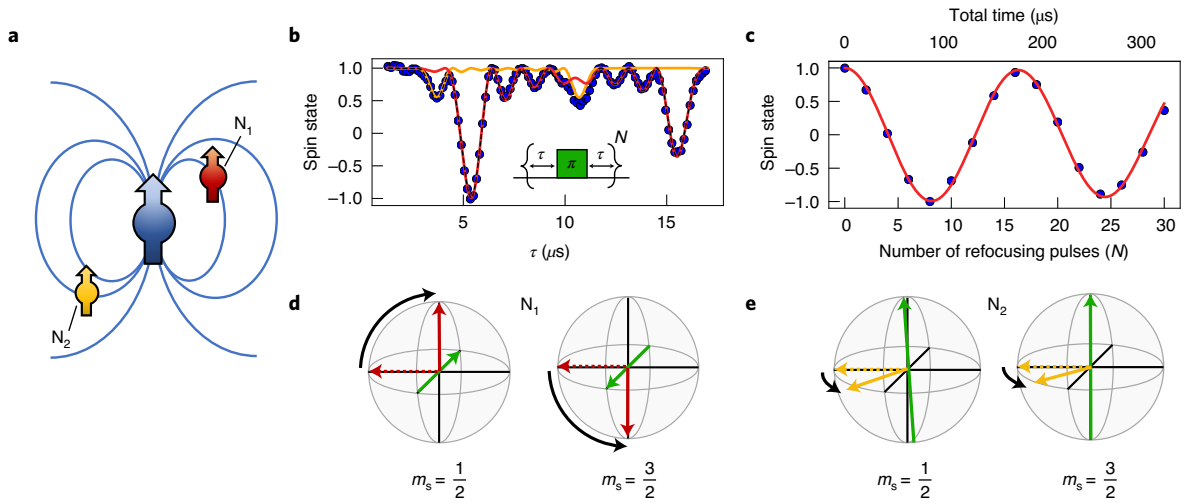

Fig. 4 | Control over nuclear spin qubits. a, Artistic representation of the coupled electron–nuclear spin triplet identified in a waveguide. **b**, Spin signal for the eight-pulse CPMG sequence (inset) at $B_0 = 81$ G. Blue dots are experimental data. The red and orange lines correspond to the (independent) spin signals obtained for the first and second nucleus, respectively. The white dashed line is the product of both fits. The strongest modulation is observed for N_1 at the resonance time $\tau^{(k)}_{\text{approx}} = 5.38$ μs. **c**, Electron spin signal for different number N of refocusing pulses at $\tau_{\text{CPMG}} = 5.38$ μs. Strong oscillations stem from electron spin-dependent rotations of N_1. Blue dots are uncorrected raw data. The red curve is a simulation based on two nuclear spins without any free parameters. In all plots, spin state +1 corresponds to $m_S = \frac{3}{2}$ and −1 to $m_S = \frac{1}{2}$. **d**, Bloch-sphere representation showing the dynamics of the nuclear spin N_1 during the $N = 4$ pulse CPMG sequence. The rotation axes (green arrows) for the electron spin states $m_S = \frac{1}{2}$ and $m_S = \frac{3}{2}$ are antiparallel ($\pm\mathbf{e}_x$) with a rotation angle of $\pm\frac{\pi}{2}$ rad. **e**, Same as in Fig. 4d, but for the nuclear spin N_2. The nuclear spin is decoupled from the electron spin as the rotation axis is (nearly) the same ($\sim\mathbf{e}_z$) with a very small rotation angle of 0.04 rad (the shown rotation is exaggerated for clarity).

are less affected than optical properties; however, ion implantation and waveguide nanofabrication can still lead to an increased abundance of parasitic spin defects[13,49]. To allow selective addressing of the three ground-state spin transitions via the MW drive, we lift the Kramers degeneracy by applying an external magnetic field of $B_0 = 36$ G along the crystal's c axis (Fig. 3a). We then deterministically initialize the spin state[29], here into $m_S = +\frac{1}{2}$, followed by probing dephasing and coherences between the levels $m_S = +\frac{1}{2}$ and $m_S = +\frac{3}{2}$.

Ramsey interferometry shows a dephasing time of $T^*_{2,\text{implanted}} = 34 \pm 4$ μs for the ion-implanted defects (Fig. 3b), which is comparable to deep-bulk defects in similar SiC crystals[15,29]. Figure 3c shows the data for V2 centres in waveguides. We find $T^*_{2,\text{waveguide}} = 9.4 \pm 0.7$ μs, which is only twice as short as compared to deep-bulk defects in the same sample, $T^*_{2,\text{bulk}} = 21 \pm 1$ μs (Section 2F of the Supplementary Information and Supplementary Fig. 12).

Hahn echo measurements with ion-implanted V2 centres are presented in Fig. 3d, showing a coherence time of $T_{2,\text{implanted}} = 1.39 \pm 0.10$ ms. This is a very long Hahn echo coherence for this system. Figure 3e shows the data for defects in waveguides, resulting in $T_{2,\text{waveguide}} = 0.84 \pm 0.01$ ms, which is comparable to bulk defects in the same sample, $T_{2,\text{bulk}} = 0.85 \pm 0.03$ ms (Section 2F of the Supplementary Information and Supplementary Fig. 12). Thus, RIE can be used for nanofabrication of high-quality SiC material without deteriorating spin properties.

Interestingly, the data in Fig. 3e display a strong modulation due to dipolar interaction with weakly coupled nuclear spins. This indicates that the hyperfine coupling strength with at least one nucleus is comparable to the Larmor frequency. We show now that the system is described by one V2 centre coupled to two nuclear spins, as depicted in the artistic design in Fig. 4a. To infer the coupling strengths with high resolution, we apply a slightly increased magnetic field, $B_0 = 81$ G and perform eight-pulse Carr–Purcell–Meiboom–Gill (CPMG) sequences with varying waiting time τ_{CPMG}. From the modulation signal in Fig. 4b, we extract that both nuclei are ^{29}Si spins with hyperfine coefficients of $A_{\parallel,1} = 2\pi \times (-23.5)$ kHz and $A_{\perp,1} = 2\pi \times 12.0$ kHz for the first nuclear spin (N_1), as well as $A_{\parallel,2} = 2\pi \times 0.2$ kHz and $A_{\perp,2} = 2\pi \times 8.5$ kHz for the second one (N_2; Supplementary Information).

Having determined the coupling coefficients, we now show coherent manipulation of an electron–nuclear spin pair in a SiC waveguide. Compared to previous work[15,50,51], we implement spin control sequences at a low magnetic field ($B_0 = 81$ G). This keeps the hyperfine coupling strength comparable to the nuclear spin Larmor frequency ω_L, which allows us to perform nuclear spin quantum gates in short times using a moderate number of CPMG pulses.

As the V2 centre ground state is a quartet, it directly provides three exploitable spin subspaces ($m_S = \left[+\frac{3}{2}; +\frac{1}{2}\right]$, $m_S = \left[+\frac{1}{2}; -\frac{1}{2}\right]$ and $m_S = \left[-\frac{1}{2}; -\frac{3}{2}\right]$) that allow us to implement vastly different nuclear spin control sequences. Here, we focus on the subspace $m_S = \left[+\frac{3}{2}; +\frac{1}{2}\right]$ to demonstrate nuclear spin rotations around the x axis for the first nuclear spin. The strong resonance signal in Fig. 4b at $\tau_{\text{CPMG}} = 5.38$ μs already indicates that electron and nuclear spins are flipped. Ensuring precise rotations around the desired x axis requires determination of the optimal waiting times $\tau^{(k)}$ (dubbed as resonances), at which the electron spin signal due to the nuclear spin precession is exactly commensurate with the CPMG pulse spacing. To this end, we develop a generalized theoretical model to describe CPMG resonances for weakly coupled nuclear spins[50] in small magnetic fields (Supplementary Information). For each individual nuclear spin, the resonances occur at

$$\tau^{(k)}_{\text{approx}} = \tau_k \left(1 + \sin\left(\frac{\omega_{1/2}\tau_k}{2}\right) \frac{(\mathbf{n}_{1/2} \cdot \mathbf{n}_{3/2})^{-1} - 1}{(2k-1)\,\pi}\right).$$

Here, the integer number k indicates the resonance number, $\tau_k = \frac{(2k-1)\pi}{\omega_{1/2}+\omega_{3/2}}$, $\omega_{m_S} = \sqrt{(m_S A_\perp)^2 + \left(m_S A_\parallel - \omega_L\right)^2}$ and $\omega_{m_S}\mathbf{n}_{m_S} = m_S A_\perp \mathbf{e}_x + \left(m_S A_\parallel - \omega_L\right)\mathbf{e}_z$. The unit vectors $\mathbf{e}_x$ and $\mathbf{e}_z$ denote the nuclear spin rotation axes. For the first resonance, we calculate $\tau^{(1)}_{\text{approx}} = 5.38$ μs, in excellent agreement with the experimental data. We now control the nuclear spin rotation angle by

varying the number N of CPMG pulses at $\tau_{CPMG} = 5.38$ µs. The uncorrected raw data in Fig. 4c reveal that the electron spin signal is modulated due to electron spin-controlled nuclear spin rotations with near-unity fringe contrast, in excellent accord with the simulated signal with no free parameters (Supplementary Information). By varying the number of refocusing pulses, we implement relevant quantum gates on the bi-partite system. The Bloch spheres in Fig. 4d visualize the electron spin-dependent rotation of the first nucleus N_1 for $N = 4$ CPMG pulses. The net result is an opposite rotation around the x axis, which can be used to implement an entangling Hadamard gate. Figure 4e shows the rotation of the second nucleus N_2. The nuclear spin is decoupled as its rotation is (essentially) independent of the electron spin state. By increasing the number of refocusing pulses, we can rotate N_1 to implement additional gates, such as the σ_x gate for $N = 8$, and the identity operation for $N = 16$. For the three gates (the Hadamard, σ_x and identity), our simulations show fidelities of 97%, 94% and 98%, respectively (Supplementary Information). These high fidelities are in part due to the fast implementation of gates using only a small number of refocusing pulses for which electron spin decoherence is negligible. In this sense, we emphasize that the small signal decrease in Fig. 4c for high pulse numbers ($N > 20$) is not associated with electron spin decoherence. The signal decrease stems from a minimal remaining spin-dependent rotation of N_2, which can be suppressed with stronger external magnetic fields[7,15]. Our results underline that waveguide-integrated V2 centres can be used for controlling nuclear spins with high fidelities at cryogenic temperatures, promising implementation of quantum memories, quantum error correction and (distributed) quantum computational tasks.

Outlook

We demonstrated that V2 centres in 4H-SiC can be successfully integrated into nanofabricated waveguide devices produced by RIE techniques. We showed further that low-energy He^+ implantation creates shallow V2 centres with high yield and good spatial accuracy. Despite using SiC crystals from completely different growth processes, we observed nearly lifetime-limited absorption lines and reported record Hahn echo electron spin-coherence times. The fact that ideally oriented V2 centres in new *a* plane 4H-SiC can be used for quantum applications offers a unique potential to further scale up of semiconductor quantum technologies[44].

To induce these steps, we outlined how to combine ideal photonic waveguide designs and implantation strategies that could be used towards realizing cavity-based spin–photon interfaces with high cooperativities[11]. For maximum coupling efficiency, such devices could be directly connected to optical fibres[52].

To interfere multiple emitters, Stark shift tuning[53] could be used for both matching resonance frequencies and shaping optical linewidths[54]. On-chip wavelength conversion to the telecom band could be implemented by utilizing the $\chi^{(2)}$ and $\chi^{(3)}$ nonlinearities of 4H-SiC[55], ultimately enabling large-scale memory-enhanced quantum repeater networks[46].

To scale up such networks, nuclear spin quantum memories and processors represent a critical technology[4]. In this sense, we demonstrated coherent control over individual nuclear spins and we implemented relevant quantum gates with high fidelity. The amount of controllable nuclear spins can be directly scaled up in isotopically engineered samples[15]. In this regard, V2 centres are very promising central spins as they can be operated at temperatures of up to $T = 20$ K before experiencing spin-optical coherence degradation[26]. The high cooling powers of standard cryogenic equipment at these temperatures make it possible to operate experiments at full duty cycle while controlling nuclear spins with high-power radiofrequency drives.

Overall, these results corroborate that V2 centres in SiC are attractive for developing large-scale quantum networks based on integrated quantum computational clusters with efficient spin–photon interfaces.

Online content

Any methods, additional references, Nature Research reporting summaries, source data, extended data, supplementary information, acknowledgements, peer review information; details of author contributions and competing interests; and statements of data and code availability are available at https://doi.org/10.1038/s41563-021-01148-3.

Received: 14 May 2021; Accept3ed: 30 September 2021;
Published online: 18 November 2021

References

1. Buhrman, H., Cleve, R., Massar, S. & De Wolf, R. Nonlocality and communication complexity. *Rev. Mod. Phys.* **82**, 665–698 (2010).
2. Barz, S. et al. Demonstration of blind quantum computing. *Science* **335**, 303–309 (2012).
3. Gottesman, D., Jennewein, T. & Croke, S. Longer-baseline telescopes using quantum repeaters. *Phys. Rev. Lett.* **109**, 070503 (2012).
4. Borregaard, J. et al. One-way quantum repeater based on near-deterministic photon-emitter interfaces. *Phys. Rev. X* **10**, 021071 (2020).
5. Atatüre, M., Englund, D., Vamivakas, N., Lee, S. Y. & Wrachtrup, J. Material platforms for spin-based photonic quantum technologies. *Nat. Rev. Mater.* **3**, 38–51 (2018).
6. Awschalom, D. D., Hanson, R., Wrachtrup, J. & Zhou, B. B. Quantum technologies with optically interfaced solid-state spins. *Nat. Photon.* **12**, 516–527 (2018).
7. Pompili, M. et al. Realization of a multi-node quantum network of remote solid-state qubits. *Science* **372**, 259–264 (2021).
8. Waldherr, G. et al. Quantum error correction in a solid-state hybrid spin register. *Nature* **506**, 204–207 (2014).
9. Kalb, N. et al. Entanglement distillation between solid-state quantum network nodes. *Science* **356**, 928–932 (2017).
10. Rozpędek, F. et al. Near-term quantum-repeater experiments with nitrogen-vacancy centers: overcoming the limitations of direct transmission. *Phys. Rev. A* **99**, 052330 (2019).
11. Janitz, E., Bhaskar, M. K. & Childress, L. Cavity quantum electrodynamics with color centers in diamond. *Optica* **7**, 1232–1252 (2020).
12. Bracher, D. O., Zhang, X. & Hu, E. L. Selective Purcell enhancement of two closely linked zero-phonon transitions of a silicon carbide color center. *Proc. Natl Acad. Sci. USA* **114**, 4060–4065 (2017).
13. Crook, A. L. et al. Purcell enhancement of a single silicon carbide color center with coherent spin control. *Nano Lett.* **20**, 3427–3434 (2020).
14. Abobeih, M. H. et al. Atomic-scale imaging of a 27-nuclear-spin cluster using a quantum sensor. *Nature* **576**, 411–415 (2019).
15. Bourassa, A. et al. Entanglement and control of single nuclear spins in isotopically engineered silicon carbide. *Nat. Mater.* **19**, 1319–1325 (2020).
16. Myers, B. A. et al. Probing surface noise with depth-calibrated spins in diamond. *Phys. Rev. Lett.* **113**, 027602 (2014).
17. Sangtawesin, S. et al. Origins of diamond surface noise probed by correlating single-spin measurements with surface spectroscopy. *Phys. Rev. X* **9**, 031052 (2019).
18. Riedel, D. et al. Deterministic enhancement of coherent photon generation from a nitrogen-vacancy center in ultrapure diamond. *Phys. Rev. X* **7**, 031040 (2017).
19. Ruf, M., Weaver, M. J., Van Dam, S. B. & Hanson, R. Resonant excitation and Purcell enhancement of coherent nitrogen-vacancy centers coupled to a Fabry-Perot microcavity. *Phys. Rev. Appl.* **15**, 024049 (2021).
20. Schröder, T. et al. Quantum nanophotonics in diamond [Invited]. *J. Opt. Soc. Am. B* **33**, B65–B83 (2016).
21. Chu, Y. et al. Coherent optical transitions in implanted nitrogen vacancy centers. *Nano Lett.* **14**, 1982–1986 (2014).
22. Burek, M. J. et al. Fiber-coupled diamond quantum nanophotonic interface. *Phys. Rev. Appl.* **8**, 024026 (2017).
23. Bradac, C., Gao, W., Forneris, J., Trusheim, M. E. & Aharonovich, I. Quantum nanophotonics with group IV defects in diamond. *Nat. Commun.* **10**, 5625 (2019).
24. Nguyen, C. T. et al. Quantum network nodes based on diamond qubits with an efficient nanophotonic interface. *Phys. Rev. Lett.* **123**, 183602 (2019).
25. Nguyen, C. T. et al. An integrated nanophotonic quantum register based on silicon-vacancy spins in diamond. *Phys. Rev. B* **100**, 165428 (2019).
26. Udvarhelyi, P. et al. Vibronic states and their effect on the temperature and strain dependence of silicon-vacancy qubits in 4H-Si C. *Phys. Rev. Appl.* **13**, 054017 (2020).

27. Udvarhelyi, P. et al. Spectrally stable defect qubits with no inversion symmetry for robust spin-to-photon interface. *Phys. Rev. Appl.* **11**, 044022 (2019).
28. Simin, D. et al. Locking of electron spin coherence above 20 ms in natural silicon carbide. *Phys. Rev. B* **95**, 161201 (2017).
29. Nagy, R. et al. High-fidelity spin and optical control of single silicon-vacancy centres in silicon carbide. *Nat. Commun.* **10**, 1954 (2019).
30. Morioka, N. et al. Spin-controlled generation of indistinguishable and distinguishable photons from silicon vacancy centres in silicon carbide. *Nat. Commun.* **11**, 2516 (2020).
31. Ohshima, T. et al. Creation of silicon vacancy in silicon carbide by proton beam writing toward quantum sensing applications. *J. Phys. D: Appl. Phys.* **51**, 333002 (2018).
32. Pavunny, S. P. et al. Arrays of Si vacancies in 4H-SiC produced by focused Li ion beam implantation. *Sci. Rep.* **11**, 3561 (2021).
33. Chen, Y. C. et al. Laser writing of scalable single color centers in silicon carbide. *Nano Lett.* **19**, 2377–2383 (2019).
34. Wang, J. F. et al. On-Demand generation of single silicon vacancy defects in silicon carbide. *ACS Photonics* **6**, 1736–1743 (2019).
35. Majety, S. et al. Quantum photonics in triangular-cross-section nanodevices in silicon carbide. *J. Phys.: Photonics* **3**, 034008 (2021).
36. Shang, Z. et al. Local vibrational modes of Si vacancy spin qubits in SiC. *Phys. Rev. B* **101**, 144109 (2020).
37. Kraus, H. et al. Room-temperature quantum microwave emitters based on spin defects in silicon carbide. *Nat. Phys.* **10**, 157–162 (2014).
38. Banks, H. B. et al. Resonant optical spin initialization and readout of single silicon vacancies in 4H-SiC. *Phys. Rev. Appl.* **11**, 024013 (2019).
39. Fuchs, F. et al. Engineering near-infrared single-photon emitters with optically active spins in ultrapure silicon carbide. *Nat. Commun.* **6**, 7578 (2015).
40. Evans, R. E., Sipahigil, A., Sukachev, D. D., Zibrov, A. S. & Lukin, M. D. Narrow-linewidth homogeneous optical emitters in diamond nanostructures via silicon ion implantation. *Phys. Rev. Appl.* **5**, 044010 (2016).
41. Ishikawa, T. et al. Optical and spin coherence properties of nitrogen-vacancy centers placed in a 100 nm thick isotopically purified diamond layer. *Nano Lett.* **12**, 2083–2087 (2012).
42. Yan, F. F. et al. Room-temperature coherent control of implanted defect spins in silicon carbide. *npj Quantum Inf.* **6**, 38 (2020).
43. Van Dam, S. B. et al. Optical coherence of diamond nitrogen-vacancy centers formed by ion implantation and annealing. *Phys. Rev. B* **99**, 161203 (2019).
44. Lukin, D. M. et al. 4H-silicon-carbide-on-insulator for integrated quantum and nonlinear photonics. *Nat. Photon.* **14**, 330–334 (2020).
45. Radulaski, M. et al. Scalable quantum photonics with single color centers in silicon carbide. *Nano Lett.* **17**, 1782–1786 (2017).
46. Bhaskar, M. K. et al. Experimental demonstration of memory-enhanced quantum communication. *Nature* **580**, 60–64 (2020).
47. Hensen, B. et al. Loophole-free Bell inequality violation using electron spins separated by 1.3 kilometres. *Nature* **526**, 682–686 (2015).
48. Dory, C. et al. Inverse-designed diamond photonics. *Nat. Commun.* **10**, 3309 (2019).
49. Rugar, A. E. et al. Narrow-linewidth tin-vacancy centers in a diamond waveguide. *ACS Photonics* **7**, 2356–2361 (2020).
50. Taminiau, T. H. et al. Detection and control of individual nuclear spins using a weakly coupled electron spin. *Phys. Rev. Lett.* **109**, 137602 (2012).
51. Taminiau, T. H., Cramer, J., Van Der Sar, T., Dobrovitski, V. V. & Hanson, R. Universal control and error correction in multi-qubit spin registers in diamond. *Nat. Nanotechnol.* **9**, 171–176 (2014).
52. Burek, M. J. et al. Fiber-coupled diamond quantum nanophotonic interface. *Phys. Rev. Appl.* **8**, 024026 (2017).
53. Rühl, M., Bergmann, L., Krieger, M. & Weber, H. B. Stark tuning of the silicon vacancy in silicon carbide. *Nano Lett.* **20**, 658–663 (2020).
54. Lukin, D. M. et al. Spectrally reconfigurable quantum emitters enabled by optimized fast modulation. *npj Quantum Inf.* **6**, 80 (2020).
55. Guidry, M. A. et al. Optical parametric oscillation in silicon carbide nanophotonics. *Optica* **7**, 1139–1142 (2020).
56. Nagy, R. et al. Narrow inhomogeneous distribution of spin-active emitters in silicon carbide. *Appl. Phys. Lett.* **118**, 044001 (2021).

Methods

Sample preparation. We used two different samples for the implantation and waveguide experiments.

For the implantation experiments, we used a 110-µm-thick 4H-^{28}Si^{12}C silicon carbide layer that was grown by chemical vapour deposition on the *c* plane of a n-type (0001) 4H-SiC wafer. The isotope purity was estimated to be [^{28}Si] > 99.85% and [^{12}C] > 99.98%, which was confirmed by secondary ion mass spectroscopy for one of the wafers in the series. After chemical mechanical polishing of the top layer, the substrate was removed by mechanical polishing and the final isotopically enriched free-standing layer had a thickness of ~100 µm. Current–voltage measurements at room temperatures showed that the layer is n-type with a free carrier concentration of $\sim 6 \times 10^{13}\,cm^{-3}$. This value is close to the concentration of shallow nitrogen donors of $\sim 4 \times 10^{13}\,cm^{-3}$, which was determined by photoluminescence at low temperatures. Deep level transient spectroscopy measurements showed that the dominant electron trap in the layer is related to the carbon vacancy with a concentration in the mid $10^{12}\,cm^{-3}$ range. Minority carrier lifetime mapping of the carrier showed a homogeneous carrier lifetime of ~0.6 µs. Since the lifetime was measured by an optical method with high injection, the real lifetime is expected to be double that, so ~1.2 µs. Such a high minority carrier lifetime indicates that the density of all electron traps should not be more than mid $10^{13}\,cm^{-3}$. To investigate colour centres from the *a* side of the samples, they were cleaved to obtain a reasonably smooth surface morphology. Samples were investigated with fluorescence microscopy and no defect centres were found.

For the waveguide experiments, we used a 28-µm-thick 4H-^{28}Si^{12}C silicon carbide layer that was grown by chemical vapour deposition on an *a*-plane n-type 4H-SiC wafer. Isotope concentration is estimated to be similar to the above-described *c*-plane samples. However, we found an increased incorporation of nitrogen donors in the $\sim 3 \times 10^{15}\,cm^{-3}$ range, which attributes to slightly increased optical linewidths. The surface roughness of this sample was measured to be below 0.4 nm via an atomic force microscope. Defects in this sample were generated using electron irradiation at 2 MeV with a fluence of 2 kGy. After irradiation, the sample was annealed at a temperature of 600 °C for 30 min to remove some interstitial-related defects.

Spin manipulation. For all spin manipulation experiments, MW was provided through a 50-µm-diameter copper wire that was placed within a 50–100 µm distance from the investigated colour centres. MW signals were generated using signal generators (Rohde & Schwarz SMIQ03b and SMIQ02b) and subsequent switches (MiniCircuits ZASWA-2–50DRA+). MW signals were combined using MW splitters, followed by a 20 dB amplifier stage. Typical MW power levels at the wire were 15–20 dBm.

He implantation process. To generate defects via He^+ ion implantation, we spin-coated a 200-nm-thick 200 K PMMA layer. Electron beam lithography was carried out in a Raith Eline apparatus with 20 kV acceleration voltage, 10 µm aperture and an exposure dose of 270 $\mu C\,cm^{-2}$. After exposure, the sample was placed in a micro-beam implanter (ion gun) with a He^+ source and a Wien filter. He^+ ions were accelerated at 6 keV and implanted into the sample at a dose of 10^{11} ions cm^{-2}. After removing the PMMA mask, the sample was annealed at 600 °C for 30 min in argon atmosphere to remove some interstitial-related defects.

RIE process. To create suspended waveguide structures, a double-layer PMMA mask (950 K and 200 K) was patterned using electron beam lithography. A 200-nm-thick nickel mask was evaporated onto the surface of the sample. The pattern was transferred onto SiC via a SF_6 plasma etching process (20 sccm, 7.5 mTorr, −20 °C, RIE power of 100 W). After completing straight and angled etching processes, mask residuals were removed by immersion into diluted nitric acid (HNO_3). Thereafter, the sample was annealed at 600 °C for 30 min in argon atmosphere to remove some interstitial-related defects.

Photonic modelling. To model the light propagation in SiC waveguides, we used finite-difference time-domain simulations in Lumerical 2020a software. Colour centres were simulated as horizontally oriented point dipoles at 917 nm, placed inside triangular waveguides with $n = 2.6$ refractive index and mesh size of 20 nm. Mode coupling was monitored for six lowest energy modes supported in the waveguide and coupling efficiencies were evaluated after 10 µm of propagation.

Data availability

Source data are provided with this paper and at https://doi.org/10.18419/darus-2107. Any further data are available from the corresponding author upon request.

Code availability

Fits to the data were made using Python software. The fit functions, parameters and simulations of hyperfine interactions can be made available upon request.

Acknowledgements

C.B., F.K. and J.W. thank A. Weible, R. Reuter, A. Zechmeister, J. Meinel, R. Nagy, J. Körber, M. Krumrein, M. Joliffe, M. Niethammer, I. Gediz, J. Zatsch, D. Dasari, Y.-C. Chen, K.-M. Fu, D. Lukin and J. Vučković for experimental assistance and fruitful discussions. We further acknowledge technical support from Swabian Instruments GmbH and Toptica Photonics AG. G.V.A. thanks U. Kentsch for the proton implantation assistance and support from the Ion Beam Centre at Helmholtz-Zentrum Dresden-Rossendorf (HZDR). N.T.S. acknowledges the Swedish Research Council (grant no. VR 2016-04068). J.U.-H. acknowledges the Swedish Energy Agency (grant no. 43611-1) and Swedish Research Council (grant no. 2020-05444). N.T.S. and J.U.-H. thank the EU H2020 project QuanTELCO (grant no. 862721) and the Knut and Alice Wallenberg Foundation (grant no. KAW 2018.0071). S.M. acknowledges support by the UC Davis Summer GSR Award. M.R. acknowledges support by the National Science Foundation under the grant CAREER-2047564. J.W. acknowledges the EU-FET Flagship on Quantum Technologies through the project ASTERIQS (grant agreement no. 820394), the European Research Council (ERC) grant SMel, the Max Planck Society and the German Research Foundation (SPP 1601, FOR 2724). F.K. and J.W. acknowledge support by the EU-FET Flagship on Quantum Technologies through the project QIA (grant agreement no. 820445), as well as the German Federal Ministry of Education and Research (BMBF) for the project Q.Link.X (grant agreement no. 16KIS0867).

Author contributions

C.B. and F.K. conceived the experiments. F.K. and J.W. directed the research. R.S., T.L., R.W. and A.D. produced masks and performed helium ion implantation. C.G. and P.B. performed helium implantation simulations. R.S., T.L., R.W. and G.V.A. produced masks and designed proton implantation. M.H. performed silicon ion implantation. W.K. performed electron irradiation. C.B., R.S. and T.L. produced SiC waveguides. V.V., S.M., P.S. and M.R. simulated beam profiles in waveguides. N.T.S. and J.U.-H. grew the SiC samples. C.B., N.M., T.L., T.S., R.W., D.L., E.H. and F.K. performed the experiments. C.B., N.M., T.L., T.S., D.L. and F.K. developed and improved software. C.B., R.W. and F.K. analysed the data. C.B. and F.K. developed the theoretical framework for nuclear spin control. C.B., M.R., F.K. and J.W. wrote the manuscript. All authors provided helpful comments during the writing process.

Competing interests

The authors declare no competing interests.

Additional information

Supplementary information The online version contains supplementary material available at https://doi.org/10.1038/s41563-021-01148-3.

Correspondence and requests for materials should be addressed to Florian Kaiser.

Peer review information *Nature Materials* thanks the anonymous reviewers for their contribution to the peer review of this work.

Reprints and permissions information is available at www.nature.com/reprints.